Nano Research

ISSN 1998-0124 CN 11-5974/O4
https://doi.org/10.26599/NR.2026.94909023

Research Article

Polarization-tunable vdW ferroelectric heterojunction for high-gain photodetection and intelligent visual recognition

Ran Ma[1], Qiuhong Tan[1,2](✉), Peizhi Yang[3], Yingkai Liu[1,2], Qianjin Wang[1,2](✉)

[1] College of Physics and Electronic Information, Yunnan Normal University, Kunming 650500, China

[2] Yunnan Provincial Key Laboratory for Photoelectric Information Technology, Yunnan Normal University, Kunming 650500, China

[3] Key Laboratory of Advanced Technique & Preparation for Renewable Energy Materials, Ministry of Education, Yunnan Normal University, Kunming 650500, China

Nano Res., **Just Accepted Manuscript** • https://doi.org/10.26599/NR.2026.94909023
https://www.sciopen.com/journal/1998-0124 on Jul. 13, 2026

Just Accepted

Table of Contents (TOC)

Polarization-tunable vdW ferroelectric heterojunction for high-gain photodetection and intelligent visual recognition

Ran Ma, Qiuhong Tan✉, Peizhi Yang, Yingkai Liu, Qianjin Wang✉

Yunnan Normal University, China

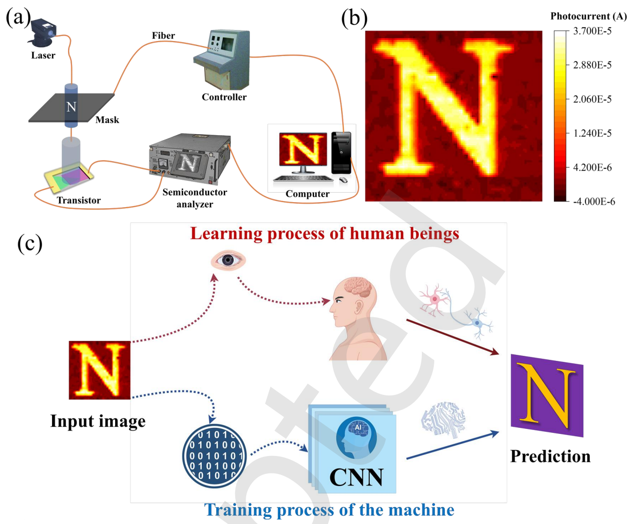

This CIPS/$CdS_{0.42}Se_{0.58}$ heterojunction photodetector exhibits outstanding photoelectric performance, neural network recognition capabilities and imaging. Achieved multi-functional integration.

Nano Research

Open Access

Research Article

Polarization-tunable vdW ferroelectric heterojunction for high-gain photodetection and intelligent visual recognition

Ran Ma [1], Qiuhong Tan [1,2], Peizhi Yang[3], Yingkai Liu[1,2], and Qianjin Wang [1,2]

[1] College of Physics and Electronic Information, Yunnan Normal University, Kunming 650500, China
[2] Yunnan Provincial Key Laboratory for Photoelectric Information Technology, Yunnan Normal University, Kunming 650500, China
[3] Key Laboratory of Advanced Technique & Preparation for Renewable Energy Materials, Ministry of Education, Yunnan Normal University, Kunming 650500, China

Received: 29 May 2026; **Revised:** 5 July 2026; **Accepted:** 13 July 2026

Address correspondence to Tan Qiuhong, tanqiuhong1@126.com; Wang Qianjin, qjwang@xtu.edu.cn

Cite this article: *Nano Research*, 2026, 19, 94909023 https://doi.org/10.26599/NR.2026.94909023

ABSTRACT: Ferroelectric phototransistors have emerged as promising platforms for integrating sensing, memory, and computing toward artificial intelligence systems, however, their practical applications are hindered by limited photoresponse and insufficient device performance. Here, we report a high-performance $CuInP_2S_6$ (CIPS)/$CdS_{0.42}Se_{0.58}$ ferroelectric heterojunction transistor enabled by a dry-transfer strategy, which synergistically combines ferroelectric polarization modulation with band-engineered heterointerfaces. The device exhibits outstanding optoelectronic performance, including a high light-to-dark current ratio of 4.37×10^5, a responsivity of 5.38×10^3 A/W, an external quantum efficiency of 1.14×10^6%, and a specific detectivity up to 3.67×10^{15} Jones, along with a fast response time of 78/320 μs. Importantly, polarization switching effectively tunes carrier transport by modulating the depletion region at the heterointerface, enabling controllable photoresponse characteristics. Leveraging these advantages, the device is further demonstrated for visible-light imaging and convolutional neural network (CNN)-assisted image recognition, achieving an accuracy of 96.09%. Compared with previously reported CIPS-based devices, this work realizes a substantial improvement in both sensitivity and speed. This study highlights the effectiveness of ferroelectric-semiconductor heterostructure engineering for high-performance photodetection and provides a viable pathway toward highly integrated and intelligent optoelectronic systems.

KEYWORDS: ferroelectric transistor, vdW heterojunction, visible light imaging, convolutional neural networks

1 Introduction

The rapid evolution of artificial intelligence (AI) and machine vision systems has stimulated an increasing demand for next-generation optoelectronic devices capable of simultaneously integrating sensing, memory, and processing functionalities [1-6]. In particular, high-performance phototransistors [7-9] with low power consumption [10-12], high integration density [13-15], and in-sensor computing capability are considered essential building blocks for neuromorphic vision systems and intelligent imaging applications [16]. However, conventional silicon-based devices are fundamentally constrained by their limited spectral response, relatively low photoelectric conversion efficiency, and high energy consumption, which hinder their application in emerging intelligent optoelectronic systems [17].

Recently, ferroelectric materials have attracted extensive attention due to their intrinsic nonvolatile polarization, atomically thin structure, and strong electrostatic tunability [18]. These unique properties enable ferroelectric field-effect transistors (FeFETs) to realize efficient carrier modulation via internal polarization fields, thereby offering new opportunities for multifunctional optoelectronic devices and in-memory computing architectures [19,20]. Among them, $CuInP_2S_6$ (CIPS), as a representative layered van der Waals ferroelectric material, exhibits room-temperature ferroelectricity, a moderate bandgap, and excellent structural stability, making it a promising candidate for photodetection and neuromorphic applications [21]. Its reversible polarization can generate a built-in electric field, thereby modulating carrier separation and transport, and is expected to enhance the device's photoresponse performance [22]. However, despite these intrinsic advantages, phototransistors based on single CIPS channels often exhibit low light-dark current ratios, limited responsivity, and insufficient signal-to-noise ratio, which significantly restrict their performance in high-resolution imaging and intelligent recognition tasks [23]. To address these challenges, various strategies have been explored, including gate engineering [24,25], defect modulation [26-28], chemical doping [29-31], and external circuit integration [32,33]. Although these approaches can partially improve device performance, they often introduce additional complexity and still face limitations in terms of noise suppression, energy efficiency, and system-level integration for neuromorphic applications.

Constructing van der Waals heterojunctions has emerged as an effective strategy to overcome these limitations by combining complementary materials and engineering interfacial band alignment [34,35]. In particular, the semiconductor alloys such as CdS_xSe_{1-x} possess tunable bandgaps, strong light absorption, and good chemical stability, making them ideal candidates for forming high-quality heterostructures with ferroelectric materials [36]. Previous studies have shown that optimizing the S/Se ratio in CdS_xSe_{1-x} alloys can effectively tailor their band structure and significantly improve photoelectric conversion efficiency, with compositions close to the equiatomic ratio generally exhibiting excellent optoelectronic properties [37]. Motivated by these findings, CdS_xSe_{1-x} alloys are considered promising candidates for constructing high-performance heterojunction photodetectors with ferroelectric semiconductors. When integrated with ferroelectric semiconductors such as CIPS, the built-in polarization field is expected to further facilitate photogenerated carrier separation, making CIPS/CdS_xSe_{1-x} heterostructures promising candidates for high-performance multifunctional optoelectronic devices.

In this work, we report a high-performance CIPS/$CdS_{0.42}Se_{0.58}$ ferroelectric heterojunction phototransistor fabricated via a dry transfer method. Benefiting from the synergistic effects of ferroelectric polarization in CIPS, the tunable bandgap of $CdS_{0.42}Se_{0.58}$ nanosheet, and the optimized interfacial band structure, the device exhibits outstanding optoelectronic performance, including a high light-to-dark current ratio of 4.37×10^5, a responsivity of 5.38×10^3 A/W, an external quantum efficiency of 1.14×10^6%, and a specific detectivity up to 3.67×10^{15} Jones, along with a fast response time of 78/320 µs. Furthermore, the device demonstrates excellent capability in visible light imaging and convolutional neural network (CNN)-based image recognition with high accuracy of 96.09%, highlighting its potential for integrated neuromorphic vision systems. This work provides an effective strategy for designing high-performance, low-power, and intelligent optoelectronic devices based on layered ferroelectric heterostructures.

2 Results and discussion

CIPS flake and $CdS_{0.42}Se_{0.58}$ nanosheet (NS) were respectively prepared by mechanical exfoliation (ME) and chemical vapor deposition (CVD) methods. The CIPS flake and $CdS_{0.42}Se_{0.58}$ NS were transferred onto the Si/SiO_2 substrate for further characterization. **Figs. 1(a)-(b)** show the UV–vis absorption spectrum of CIPS flake and $CdS_{0.42}Se_{0.58}$ NS, respectively. It can be seen that the CIPS flake and $CdS_{0.42}Se_{0.58}$ NS have strong light absorption in range 300-600 nm and 300-650 nm, respectively. According to Tauc's plot, it is expressed by the following formula $(\alpha h\nu)^n = A\,(h\nu - E_g)$ [38]. In the formula, direct bandgap semiconductor n = 2 and indirect bandgap semiconductor n = 1/2. The band gap of CIPS flake and $CdS_{0.42}Se_{0.58}$ NS can be calculated as 2.75 eV and 1.87 eV respectively, as shown in their insets. Based on the ultraviolet/visible/near-infrared light absorption diagram of Figs. 1(a)-(b), the band gap of the material can be characterized, but the method of determining the band structure is often far from sufficient through the two diagrams of Figs. 1(a)-(b). Therefore, we further studied the band structure of the materials by testing ultraviolet photoelectron spectroscopy (UPS).

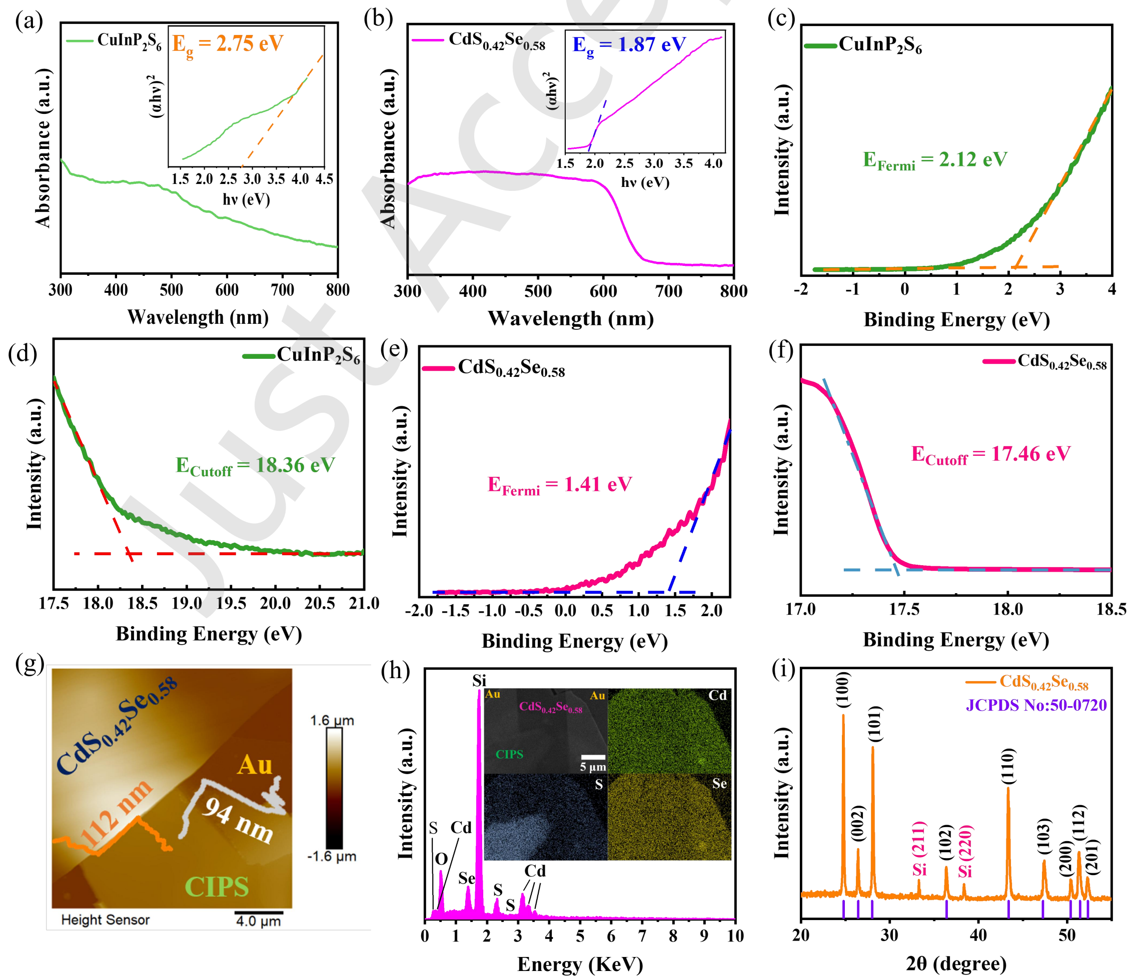

Figure 1. Ultraviolet-visible-infrared absorption spectra of (a) CIPS flake and (b) $CdS_{0.42}Se_{0.58}$ NS. Ultraviolet photoelectron spectroscopy of (c-d) CIPS flake and (e-f) $CdS_{0.42}Se_{0.58}$ NS. (g) AFM images of CIPS flake and $CdS_{0.42}Se_{0.58}$ NS. (h) EDS picture (inserted image is mapping) and (i) XRD diagram of $CdS_{0.42}Se_{0.58}$ NS.

Fig. 1(c) shows the sizes of the valence band top of CIPS flake to Fermi level. The difference between the valence band top of 2.12 eV and fermi level is extracted by linear extrapolation method. **Fig. 1(d)** shows the secondary electron cutoff energy of CIPS flake. The size of 18.36 eV was extracted, and the work function W_1 = 2.86 eV was calculated. Similarly, **Fig. 1(e)** shows the size of $CdS_{0.42}Se_{0.58}$ NS valence band top to fermi level. The difference between 1.41 eV valence band top to fermi level is extracted. **Fig. 1(f)** shows the secondary electron cutoff energy of $CdS_{0.42}Se_{0.58}$ NS. The size of 17.46 eV was extracted, and the work function W_2 = 3.76 eV was calculated. In this way, the valence band position, work function and band gap of the CIPS flake and $CdS_{0.42}Se_{0.58}$ NS are determined respectively, and their band structure diagrams can be made to explain the physical mechanism. The thickness of the material is also closely related to the performance of the semiconductor material. Therefore, the thickness of the material was characterized using atomic force microscope (AFM). **Fig. 1(g)** shows the AFM thickness of CIPS flake and $CdS_{0.42}Se_{0.58}$ NS. The surfaces of CIPS flake and $CdS_{0.42}Se_{0.58}$ NS are very slippery, with thickness of 94 nm and 112 nm respectively. The results show that $CdS_{0.42}Se_{0.58}$ prepared by CVD and CIPS of mechanical stripping have good morphology. To further verify the elemental composition of $CdS_{0.42}Se_{0.58}$, energy dispersive X-ray spectrometers (EDS) was used to characterize the elements of $CdS_{0.42}Se_{0.58}$. **Fig. 1(h)** shows the EDS of the $CdS_{0.42}Se_{0.58}$ NS, including Si, O, Cd, Se and S elements. Cd, Se and S elements are present in the $CdS_{0.42}Se_{0.58}$ NS, in which Si and O originate from the SiO_2 substrate. Inserted image shows the elemental mapping image of the $CdS_{0.42}Se_{0.58}$ NS. These elements are evenly distributed in the $CdS_{0.42}Se_{0.58}$ NS. The magnified SEM showed exceptionally smooth surfaces of the $CdS_{0.42}Se_{0.58}$ NS, demonstrating the excellent crystalline quality of the $CdS_{0.42}Se_{0.58}$ NS. To further confirm the elemental composition ratio of S and Se in $CdS_{0.42}Se_{0.58}$ NS, X-ray diffraction (XRD) characterization was conducted on it. **Fig. 1(i)** shows the XRD pattern of the $CdS_{0.42}Se_{0.58}$ NS. The 2θ peaks of the $CdS_{0.42}Se_{0.58}$ located at 24.3°, 25.9°, 27.7°, 35.8°, 42.9°, 46.9°, 49.9°, 50.8° and 51.8° correspond to (100), (002), (101), (102), (110), (103), (200), (112) and (201) crystal planes. The results show that the diffraction peak is consistent with the JCPDS No: 50-0720 standard card, in which the ratio of S to Se is 0.42:0.58. Two small peaks emerged at approximately 2θ = 33.3° and 2θ = 38.3°, which correlate to the (211) and (220) diffraction peak of the Si substrate by comparison with the JCPDS No: 17-0901 standard card.

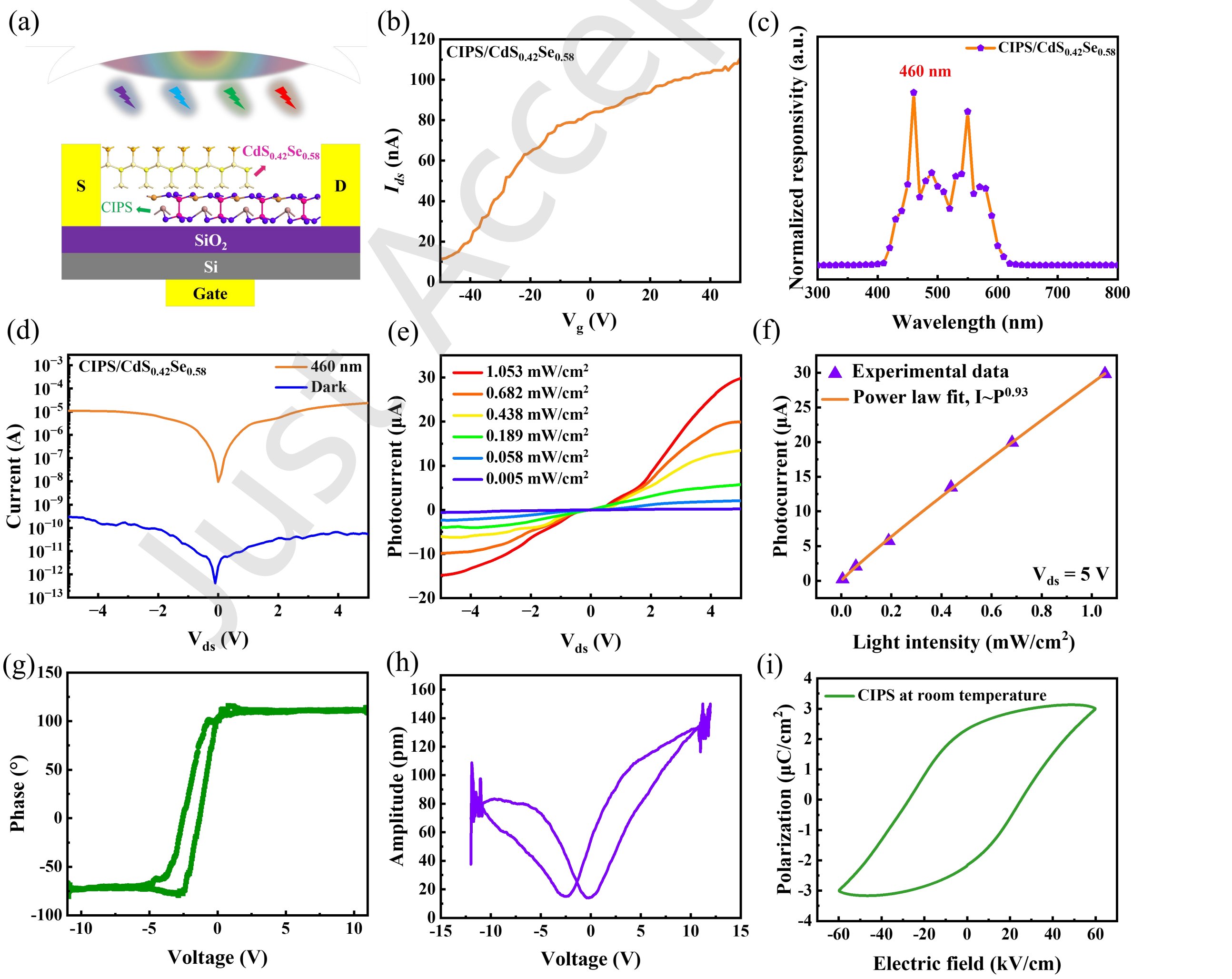

Figure 2. (a) Heterojunction device diagram, (b) transfer curve at 5 V bias, (c) spectral response curve under 5 V bias, (d) *I-V* curves under 460 nm monochromatic light and dark, (e) *I-V* curves under different LPD and (f) intensity-depended photocurrent of CIPS/$CdS_{0.42}Se_{0.58}$ heterojunction device. The hysteresis curves of (g) phase and (h) amplitude. (i) Ferroelectric hysteresis loop.

Based on the characterization results, electrical properties, photoelectric properties and the ferroelectric properties of CIPS/$CdS_{0.42}Se_{0.58}$ heterojunction were further discussed. **Fig. 2(a)** shows the schematic diagram of the heterojunction ferroelectric transistor. **Fig. 2(b)** presents the transfer curve of CIPS/$CdS_{0.42}Se_{0.58}$ heterojunction device at 5 V bias. The transfer curve demonstrated the characteristics of a n-type transistor. **Fig. 2(c)** shows the spectral response of the CIPS/$CdS_{0.42}Se_{0.58}$ heterojunction ferroelectric phototransistor ranging from 300 to 800 nm. Obviously, the heterojunction device showed a strong response to visible (410 – 610 nm) wavelengths, these results indicated that excitons contributed to the photocurrent. **Fig. 2(d)** plots the current–voltage (*I*–*V*) curve of the CIPS/$CdS_{0.42}Se_{0.58}$ heterojunction ferroelectric phototransistor under 460 nm illumination and dark. The photocurrent drastically increased with increasing bias voltage. When the bias voltage reaches 5 V, the photocurrent of the heterojunction device reaches 2.35×10^{-5} A, the dark current reaches 5.37×10^{-11} A, and the ratio of photocurrent to dark current reaches 4.37×10^{5}. These conditions indicate that the prepared heterojunction device has outstanding photoelectric performance. Hence, we further study the photoelectric performance of the heterojunction device. **Fig. 2(e)** shows the *I*–*V* curves of the CIPS/$CdS_{0.42}Se_{0.58}$ heterojunction device under different light intensities at 460 nm light illumination. Obviously, the photocurrent increased with increasing light power density (LPD) at the same bias voltage, indicating that the number of photogenerated carriers was proportional to the absorbed photon flux. When the LPD was 1.053 mW/cm^2, at 5 V bias, the photocurrent reached 2.98×10^{-5} A. **Fig. 2(f)** shows the relationship between the photocurrent and LPD of the CIPS/$CdS_{0.42}Se_{0.58}$ heterojunction device at a bias of 5 V. The power law formula is as follows: $I_p = KP^{\alpha}$ [39], where I_p is the photocurrent, K is the proportional coefficient, P is the LPD, and exponent α is the fitting coefficient and reflects the trapping and recombination activity of photocarriers. The α value was determined to be 0.93 using the above fitting formula. Minor deviations from the ideal value of 1 suggest that the device has a low density of trap states and low recombination loss [40-42]. Through the Piezoresponse Force Microscopy (PFM) test at room temperature, the ferroelectricity of CIPS was confirmed. The phase curve indicated that CIPS has a 180° polarization reversal characteristic (**Fig. 2(g)**), with an amplitude that is a nonlinear butterfly curve (**Fig. 2(h)**). Therefore, its ferroelectric properties were tested next. **Fig. 2(i)** presents the polarization-voltage (*P*-*V*) hysteresis loop of CIPS. The results show that the CIPS device has a residual polarization strength of 2.38 μC/cm^2, indicating that this device possesses excellent ferroelectric properties.

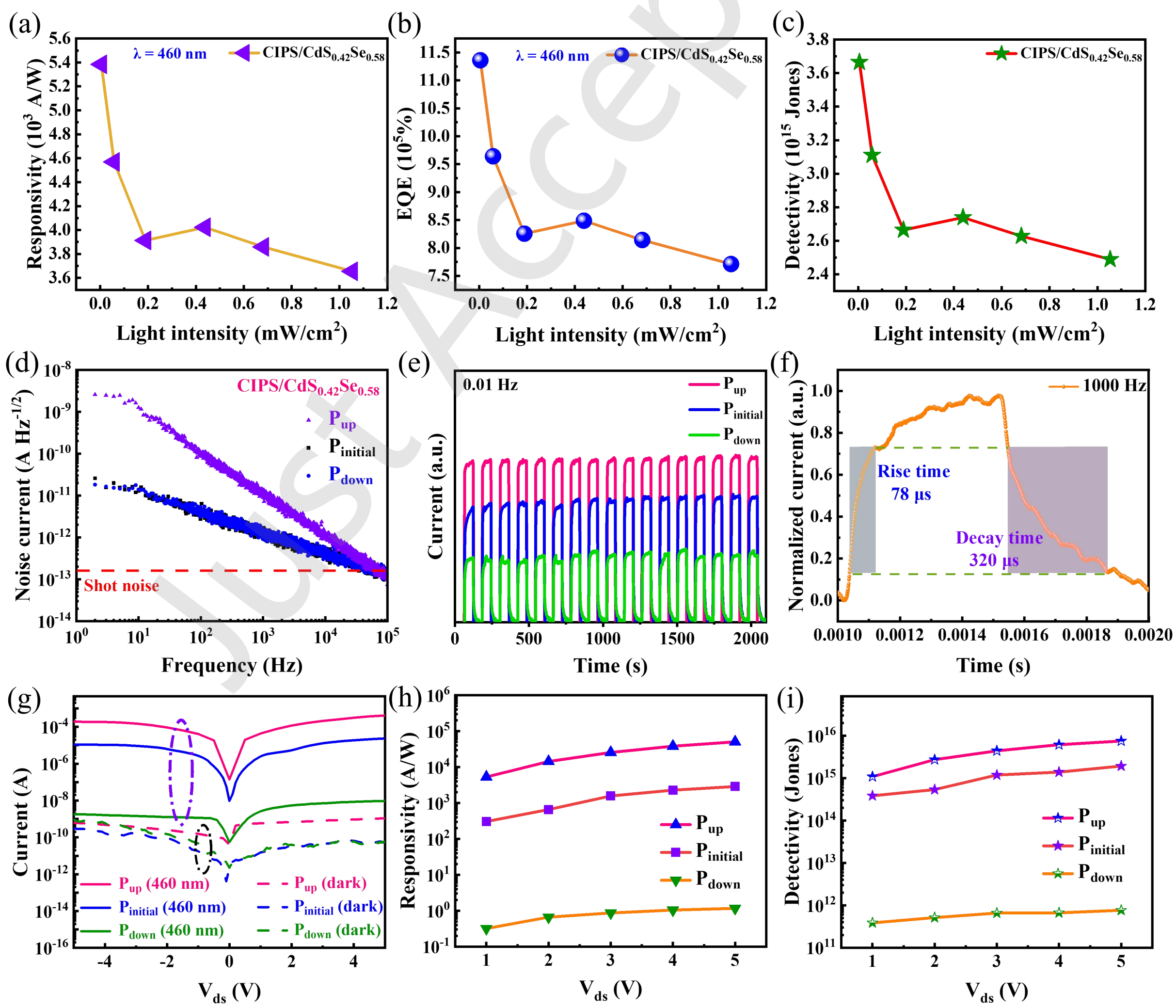

Figure 3. (a) R, (b) EQE and (c) D* of the CIPS/$CdS_{0.42}Se_{0.58}$ heterojunction device under various LPD at 5 V bias and 460 nm. (d) noise current of the CIPS/$CdS_{0.42}Se_{0.58}$ heterojunction with upward polarization, the initial state, and downward polarization. (e) The *I-t* measurement at three states and (f) response time of the CIPS/$CdS_{0.42}Se_{0.58}$ heterojunction device. The (g) *I-V* curves, (h) R, and (i) D* of the CIPS/$CdS_{0.42}Se_{0.58}$ heterojunction with upward polarization, the initial state, and downward polarization.

To further research the photoelectric performance of the CIPS/$CdS_{0.42}Se_{0.58}$ heterojunction device, some key parameters of the devices were calculated. As is well established, the R [43,44], EQE [45,46] and D^* [47-50] are three critical parameters in characterizing photodetector performance, and they can be determined using the following expressions:

$$R = \frac{I_p - I_d}{P \cdot A} \quad (1)$$

$$EQE = R\left(\frac{hc}{q\lambda}\right) \quad (2)$$

$$D^* = R\sqrt{\frac{A}{2qI_d}} \quad (3)$$

where I_p represents the photocurrent, I_d represents the dark current, P represents the LPD, A is the device area, h is Planck's constant, c is the speed of light, q is the electron charge, λ represents the incident wavelength.

According to the calculation literature [51] regarding the effective area of this device, the effective area of this heterojunction phototransistor has been calculated as 7.76×10^{-6} cm^2 (the total area of all materials between the source electrode and the drain electrode). **Figs. 3(a)-(c)** show the R, EQE and D^* of the CIPS/$CdS_{0.42}Se_{0.58}$ heterojunction device under a 5 V bias. All three parameters decreased with increasing LPD, which can be attributed to the enhanced recombination rate and reduced photoconductive gain at higher photogenerated carrier densities [42,52]. R, EQE and D^* had maximum values of 5.38×10^3 A/W, 1.14×10^6 % and 3.67×10^{15} Jones under 5 μW/cm^2 at a 5 V bias, respectively. To avoid the potential overestimation of D^* that may arise from Equation (3), precise measurements of the frequency-modulated noise current were conducted to obtain a more reliable evaluation (**Fig. 3(d)**). The results demonstrate that the CIPS/$CdS_{0.42}Se_{0.58}$ heterojunction device exhibits typical flicker noise characteristics, while gradually approaching the shot-noise limit at higher frequencies, which can be expressed as:

$$I_{shot} = \sqrt{2qI_d} \quad (4)$$

Based on the experimentally measured noise current, the specific detectivity was calculated according to:

$$D^* = \frac{R\sqrt{AB}}{i_{noise}} \quad (5)$$

where B is the bandwidth and i_{noise} is the noise current. Notably, in the high-frequency regime (10^5 Hz), the device achieves a maximum specific detectivity of approximately 4.59×10^{15} Jones, which is in good agreement with the values estimated using Equation (3). Similarly, the maximum D^* values of the CIPS/$CdS_{0.42}Se_{0.58}$ heterojunction under upward and downward polarization states are calculated to be 4.81×10^{13} Jones and 5.32×10^{15} Jones, respectively. Even at a low frequency of 10 Hz, the device still maintains impressive D^* values of 3.76×10^{10} Jones, 3.67×10^{12} Jones, and 3.39×10^{12} Jones for the upward-polarized, initial, and downward-polarized states, respectively, highlighting its excellent photodetection capability over a wide frequency range.

In addition, long-term operational stability and rapid response speed are critical performance metrics for high-performance phototransistors. **Fig. 3(e)** shows the long-term dynamic photocurrent switching characteristics (I-t) of the CIPS/$CdS_{0.42}Se_{0.58}$ heterojunction ferroelectric photovoltaic transistor under a 0.01 Hz periodic optical modulation. To reveal the ferroelectric modulation effect in the device, the switching behaviors under three different polarization states were systematically compared. When the device was modulated to the P_{up} state, a larger photocurrent response was obtained compared to $P_{initial}$; conversely, when in the P_{down} state, a smaller photocurrent response was obtained compared to $P_{initial}$, which is consistent with the photocurrent shown in **Fig. 3(g)**. Moreover, after continuous irradiation for 2000 s in each of the three working states, the photocurrent amplitude did not show any significant attenuation, fully demonstrating the excellent working stability and reliable repeatability of the ferroelectric modulation photovoltaic response. **Fig. 3(f)** shows the response time diagram of the CIPS/$CdS_{0.42}Se_{0.58}$ heterojunction device in single on and off states under a 5 V bias. The rise time is defined as the time needed for the photocurrent to increase from 10% to 90% of the maximum value during the rising process, while the decay time is defined as the time needed for the photocurrent to decrease from 90% to 10% during the falling process in a single switch periodicity. The rise and decay times of the CIPS/$CdS_{0.42}Se_{0.58}$ heterojunction device are as short as 78/320 μs, respectively. The rapid response time of the CIPS/$CdS_{0.42}Se_{0.58}$ heterojunction device can be attributed to the good crystal quality of the CIPS flake and $CdS_{0.42}Se_{0.58}$ NS, as well as the effective interface charge separation between them. In this work, the response time of the CIPS/$CdS_{0.42}Se_{0.58}$ heterojunction device is reduced to just 78 μs, which is quite lower than the reported values in many phototransistor fields; thus, the CIPS/$CdS_{0.42}Se_{0.58}$ heterojunction device has remarkable application of visible light imaging and CNN image recognition. To investigate the modulation effect of ferroelectric polarization on carrier transport, the photocurrent and dark current were further measured under three distinct polarization states: upward polarization state, initial state, and downward polarization state, as shown in **Fig. 3(g)**. Specifically, the device current measured at V_g = 0 V without any polarization treatment is defined as the initial polarization state ($P_{initial}$). Subsequently, a gate voltage of +50 V is applied to fully polarize the CIPS layer, after which the gate voltage is returned to 0 V. The photocurrent measured under the remanent polarization is defined as the upward polarization state (P_{up}). Similarly, after applying −50 V and then returning the gate voltage to 0 V, the device remains in the downward polarization state (P_{down}) owing to the remanent ferroelectric polarization. Therefore, all photocurrent measurements were performed at V_g = 0 V, ensuring that the measured differences originate solely from the remanent ferroelectric polarization rather than the applied gate electric field. It is evident that the upwardly polarized photocurrent is higher than that in the initial state, while the downwardly polarized photocurrent is lower than that in the initial state. This indicates that an upward polarization is beneficial for enhancing the responsivity of the CIPS/$CdS_{0.42}Se_{0.58}$ device. **Figs. 3(h)-(i)** presents the responsivity and detectivity of CIPS/$CdS_{0.42}Se_{0.58}$ heterojunction devices with polarized upward, initial state, and polarized downward. Compared with the initial state, the responsivity (**Fig. 3(h)**) and detectivity (**Fig. 3(i)**) of the device in the polarized upward state are both superior to those of the initial state, while the opposite is true for the polarized downward state. These results indicate that the photoelectric performance of the CIPS/$CdS_{0.42}Se_{0.58}$ heterojunction device is greatly influenced by the polarization direction. Thus, in order to further explain the influence of the polarization direction on the device, the analysis of the electronic band structures of CIPS and $CdS_{0.42}Se_{0.58}$ can be conducted. All the calculation methods for photoelectric performance parameters strictly follow the consensus standards for emerging photodetectors [53].

Fig. 4(a) presents the scanning electron microscope image of the CIPS/$CdS_{0.42}Se_{0.58}$ heterojunction device. In the image, the yellow regions correspond to the electrodes, the green region represents CIPS, and the pink region corresponds to $CdS_{0.42}Se_{0.58}$. The channel length of each adjacent pair of Au electrodes is 10 μm. To investigate the generation and transport mechanism of the photocurrent in the CIPS/$CdS_{0.42}Se_{0.58}$ device, the photocurrent mapping was performed under a 5 V bias, as shown in **Fig. 4(b)**, which corresponds to the blue square area in Fig. 4(a). From the results of the photocurrent mapping, it can be seen that the photocurrent is mainly distributed in the overlapping area of the CIPS flake and the $CdS_{0.42}Se_{0.58}$ NS, indicating that the photogenerated electron-hole pairs have been effectively separated between the heterojunctions. These results are macroscopic experimental findings. To explain the performance improvement mechanism of the CIPS/$CdS_{0.42}Se_{0.58}$ device from a microscopic perspective, the interfacial band alignment between CIPS and $CdS_{0.42}Se_{0.58}$ was studied based on the absorption spectra and UPS characterization results in **Fig. 4(c)**. **Figs. 4(d)-(f)** schematically illustrate the carrier transport mechanisms in the heterojunction under illumination and under different polarization states. Upon formation of the heterojunction, electron diffusion creates a depletion region at the interface. When the polarization of CIPS is upward (V_g = +50 V, **Fig. 4(d)**), the depletion region narrows compared to the initial state (V_g = 0 V, **Fig. 4(e)**), facilitating carrier transport across the interface and thereby enhancing the photocurrent. Conversely, under downward polarization (V_g = -50 V, **Fig. 4(f)**), the depletion region widens, impeding carrier movement and reducing the photocurrent. Under dark conditions, the concentration of free carriers is relatively low. Compared with the P_{up} state, the $P_{initial}$ and P_{down} states exhibit a wider interfacial depletion region, resulting in a higher carrier transport barrier. Consequently, carrier transport is suppressed, leading to similarly low dark currents and nearly overlapping transfer characteristics for the $P_{initial}$ and P_{down} states (**Fig. 3(d)** and **Fig. 3(g)**). These results indicate that the direction of polarization directly modulates carrier transport within the heterojunction, which in turn governs the optical response of the device and serves as the key factor determining its photoelectric performance.

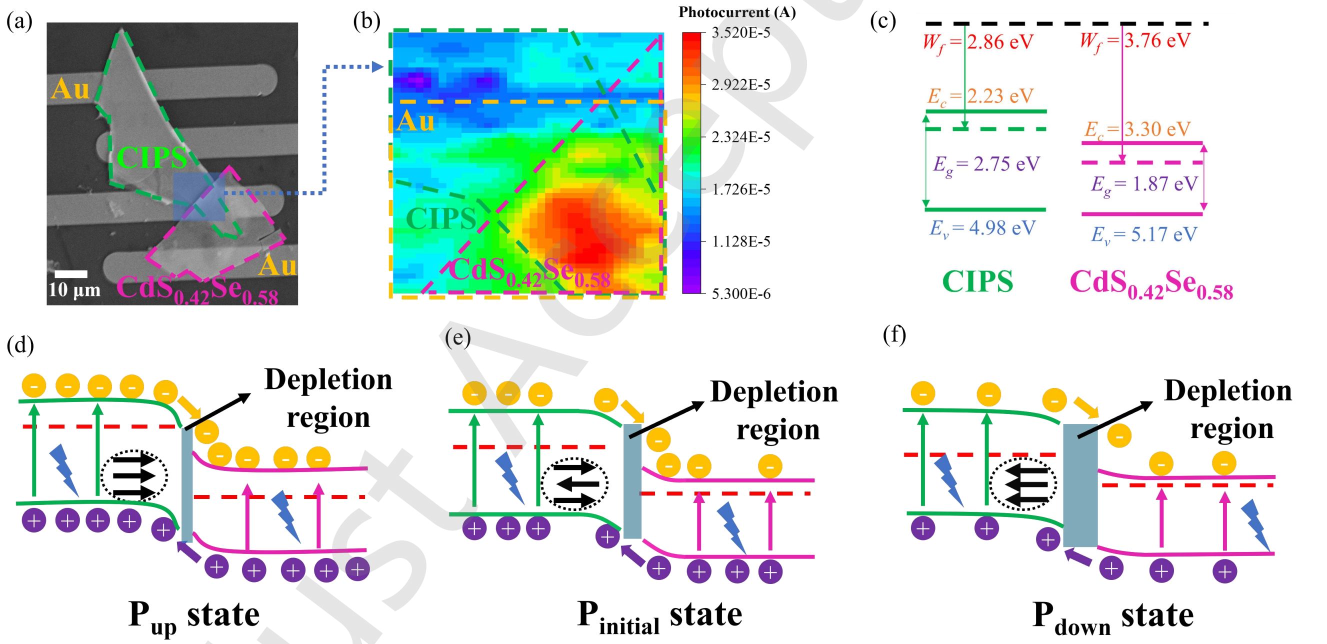

Figure 4. (a) The scanning electron microscope image of the CIPS/$CdS_{0.42}Se_{0.58}$ heterojunction device, (b) the photocurrent mapping diagram, (c) energy band diagram before heterojunction contact, under 460 nm illumination the energy band diagram under (d) polarization upward state, (e) initial state and (f) polarization downward state.

Obviously, the CIPS/$CdS_{0.42}Se_{0.58}$ heterojunction ferroelectric phototransistor exhibits outstanding ferroelectric characteristics, electrical properties, and optoelectronic performance. As is well known, the practical applications of optoelectronic devices are closely associated with their overall performance. Therefore, the device was further investigated for single-pixel imaging and CNN-based image recognition applications. The laser beam was directed through an N-shaped mask and subsequently illuminated onto the CIPS/$CdS_{0.42}Se_{0.58}$ heterojunction device. Through coordinated measurements using a semiconductor parameter analyzer and a computer-controlled imaging system, the N-shaped pattern on the mask was successfully reconstructed, as shown in **Fig. 5(a, b)**. This result demonstrates the excellent imaging capability and potential application advantages of the CIPS/$CdS_{0.42}Se_{0.58}$ heterojunction ferroelectric phototransistor in intelligent optoelectronic imaging systems. When humans observe an image, the brain can automatically process visual information and extract key features, as illustrated by the red flowchart in **Fig. 5(c)**. Similarly, CNN emulate this biological visual processing mechanism through algorithmic architectures, thereby functioning as an artificial “brain” for image analysis and recognition, as represented by the blue flowchart in **Fig. 5(c)**. To emulate biological visual processing, we conducted a system-level CNN simulation to assess the potential of the CIPS/$CdS_{0.42}Se_{0.58}$ device for future hardware-based neuromorphic vision applications. The reconstructed single-pixel imaging results were used as the input of the CNN, while the EMNIST-letters dataset was adopted to evaluate pattern recognition performance. The simulated CNN architecture, as illustrated in **Fig. 5(d)**, consists of three hierarchical convolutional blocks. Each block employs 3 × 3 convolutional kernels followed by Batch Normalization, ReLU activation, and a 2 × 2 Max Pooling layer with a stride of 2. The feature map depth progressively increases from 32 to 64 and finally to 128. To improve model robustness and suppress overfitting, Dropout layers (0.25 in convolutional blocks and 0.5 in the fully connected layer) were incorporated. The network culminates in a fully connected layer with 512 neurons, followed by a 26-node output layer for character classification, ultimately enabling accurate prediction of the reconstructed single-pixel imaging patterns. The training performance of the CNN model is presented in **Fig. 5(e)**. After 20 training epochs, the model achieved a high recognition accuracy of 96.09%, highlighting the strong potential of the proposed ferroelectric phototransistor for integrated intelligent imaging and neuromorphic vision applications. This work therefore provides a promising strategy for the development of ferroelectric transistor-based image recognition systems.

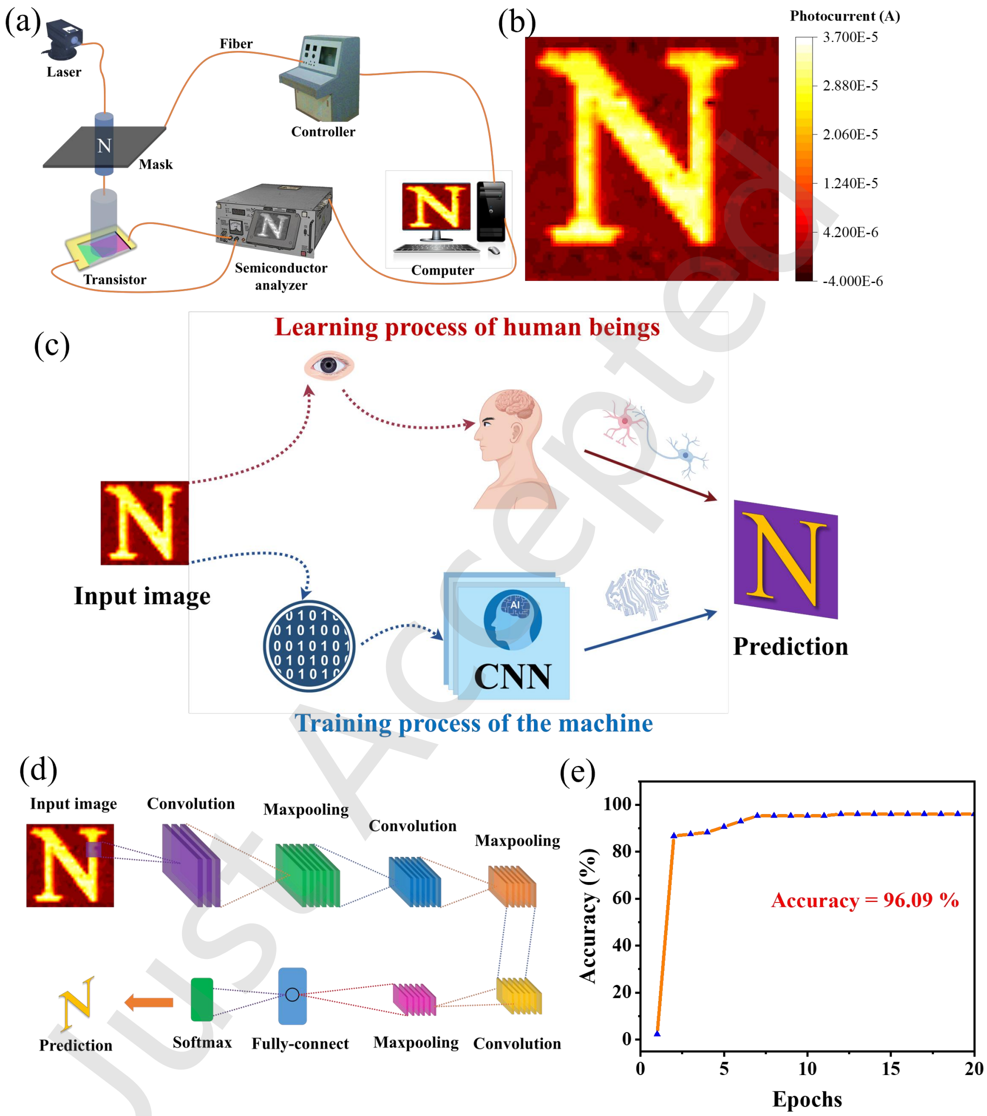

Figure 5. (a) The schematic diagram and (b) the result diagram of visible light imaging of the CIPS/$CdS_{0.42}Se_{0.58}$ heterojunction device. (c) The schematic diagram that mimics the principles of human learning, (d) the flow chart of image recognition and (e) the accuracy diagram of CNN on the EMNIST-letters dataset.

In order to facilitate comparison with other previously reported works, the key parameters of the CIPS device and its heterojunction properties were summarized. As summarized in **Table 1**, the device achieves an ultrahigh responsivity of 5.38×10^3 A/W, which is substantially higher than those of previously reported CIPS heterostructures, such as CIPS/h-BN/$MoTe_2$ (6.07 A/W) [34], WS_2/CIPS (88 A/W) [56], and CIPS/Bi_2O_2Se (339 A/W) [57]. Meanwhile, the specific detectivity reaches 10^{15} Jones, surpassing most existing CIPS-based photodetectors by several orders of magnitude, indicating its superior weak-light detection capability. In addition, the device exhibits an excellent light-to-dark current ratio (4.37×10^5), demonstrating efficient suppression of dark current and enhanced photoresponse sensitivity. More importantly, the photodetector maintains a fast response speed with rise/decay times of 78/320 μs, which are comparable to or better than many previously reported ferroelectric heterojunction photodetectors. Although the reported performance metrics were measured under different experimental conditions, the comparison indicates that our CIPS/$CdS_{0.42}Se_{0.58}$ heterojunction phototransistor exhibits competitive overall optoelectronic performance among representative CIPS-based photodetectors, particularly in terms of responsivity, detectivity, EQE, and switching ratio. The remarkable overall performance can be attributed to the synergistic effects of ferroelectric polarization modulation in CIPS, favorable type-II band alignment at the heterointerface, and efficient separation/transport of photogenerated carriers. These results demonstrate that the CIPS/$CdS_{0.42}Se_{0.58}$ heterojunction provides a highly competitive platform for high-performance ferroelectric optoelectronic devices and intelligent visual sensing applications.

Table 1. Comparison of performance parameters based on CIPS and its heterojunction devices. The reported performance metrics were extracted from the corresponding literature and measured under different experimental conditions (e.g., bias voltage, illumination wavelength, and optical power density).

Device	V_{ds} and Wavelength	R (A/W)	EQE (%)	D^* (Jones)	I_{light}/I_{dark}	Rise/Decay time (ms)	Reference
CIPS nanoflake	4 V/280 nm	0.0108	–	7.38×10^{10}	~10^3	0.36/0.44	[54]
CIPS	2.2 V/405 nm	0.0245	–	1.73×10^{11}	–	–	[23]
CIPS/h-BN/$MoTe_2$	1 V (V_g=20 V)/635 nm	6.07	1.2×10^3	5.67×10^{11}	1.2×10^4	1.8/1.26	[34]
CIPS/MoS_2	3 V/405 nm	~0.8	~0.3	~10^{10}	~2	–	[55]
WS_2/CIPS	-3 V/405 nm	88	–	3.4×10^{13}	5.2×10^4	0.0376/0.3713	[56]
CIPS/Bi_2O_2Se	2 V/550 nm	339	7.65×10^4	3.99×10^{10}	~25	2.74/4.82	[57]
CIPS/MoS_2	6 V/532 nm	321	–	4.6×10^{10}	~1.45	–	[58]
In_2Se_3/CIPS	1 V (V_g=40 V)/532 nm	41.42	–	9.79×10^{11}	~2.13	170/330	[59]
CIPS/$CdS_{0.42}Se_{0.58}$	5 V/460 nm	5.38×10^3	1.14×10^6	3.67×10^{15}	4.37×10^5	0.078/0.320	This work

3 Conclusions

In summary, a high-performance CIPS/$CdS_{0.42}Se_{0.58}$ ferroelectric heterojunction phototransistor has been successfully fabricated via a dry transfer strategy. Benefiting from the synergistic effects of ferroelectric polarization in CIPS and favorable band alignment at the heterointerface, the device exhibits significantly enhanced photoelectric performance, including an ultrahigh light–dark current ratio (4.37×10^5), high responsivity (5.38×10^3 A/W), exceptional specific detectivity (~10^{15} Jones), and fast response speed (78/320 μs). The polarization-dependent modulation of the depletion region effectively governs carrier transport, leading to reduced recombination and improved photogeneration efficiency. Furthermore, the device demonstrates excellent stability and tunability, and successfully enables visible-light imaging and CNN-based image recognition with an accuracy of 96.09%, highlighting its capability for integrating sensing, memory, and computing. Compared with previously reported CIPS-based devices, this work achieves a substantial performance breakthrough, underscoring the effectiveness of heterojunction engineering. Overall, this study not only provides insight into ferroelectric-modulated carrier dynamics in heterostructures but also offers a promising pathway toward high-integration and intelligent optoelectronic systems for next-generation neuromorphic vision applications.

4 Experimental section

4.1 Prparation of CIPS/$CdS_{0.42}Se_{0.58}$ heterojunction ferroelectric transistor.

Firstly, $CdS_{0.42}Se_{0.58}$ was prepared by the CVD method [60]. CIPS is prepared by mechanical exfoliation method. Secondly, the Ti and Au were successively deposited on the clean SiO_2 substrate as electrode with a channel length of 10 μm by using ultra-violet lithography and electron beam evaporation equipment. Thirdly, CIPS/$CdS_{0.42}Se_{0.58}$ heterojunction was constructed by respectively transferring CIPS and $CdS_{0.42}Se_{0.58}$ on Ti/Au electrodes using PDMS film. Finally, the silicon dioxide (SiO_2) dielectric layer was removed using a diamond knife to form the back-gate CIPS/$CdS_{0.42}Se_{0.58}$ heterojunction ferroelectric transistor.

4.2 Device fabrication and characterization.

The fabrication and preliminary observation of the CIPS/$CdS_{0.42}Se_{0.58}$ heterojunction were carried out using a 2D material micro-transfer system (E1-G, Metatest Corporation, China). These characterizations included the absorption spectra (Shimadzu UV-3600 Plus, Japan), AFM (Dimenson ICON, USA), UPS (Thermo Scientific Nexsa™, USA), SEM (Quanta FEG 250, USA), EDS (K-Alpha+, USA), XRD (DX-2700, China), *I-V* and *I-t* curves (Keithley 4200SCS, USA), the photocurrent mapping (MStarter 200, China), noise current (PDA FS-Pro, China), *P-E* curves (aixACCT TF2000E, Germany).

Data availability

All data needed to support the conclusions in the paper are presented in the manuscript. Additional data related to this paper may be requested from the corresponding author upon request.

Acknowledgements

This work was supported by the National Natural Science Foundation of China (Nos. 62464014, 12464025 and 12264056), the Basic Research Program of Yunnan Province (Nos. 202401AT070134), Project for Building a Science and Technology Innovation Center Facing South Asia and Southeast Asia (202403AP140015), Spring City Plan: The High-level Talent Promotion and Training Project of Kunming (2022SCP005), and Yunnan Provincial Department of Education Scientific Research Fund Project (No. 2026Y0319).

Declaration of competing interest

Please All the contributing authors report no conflict of interests in this work.

Author contribution statement

T. Q. H. and W. Q. J. came up with the initial idea and oversaw the entire project. M. R. was mainly responsible for the experimental work and the writing of the paper. The manuscript was written through the contributions of all authors. All authors have approved the final version of the manuscript.

Use of AI statement

None

References

[1] Lee, Y. H.; Lee, W. J.; Park, G. S.; Yuan, J. Y.; Won, Y.; Mun, J.; Yang, J.; Baek, S. D.; Lee, H.; Oh, J. H.; Pennycook, T. J.; Kim, G.; Mei, J.; Dou, L. Large-scale 2D perovskite nanocrystals photodetector array via ultrasonic spray synthesis. *Adv. Mater.* **2025**, *37*, 2417761.

[2] Qi, X.; Dai, S.; Chu, C.; Yu, S.; Wang, X.; Yang, S.; Ling, F. C. C.; Yang, G. Synaptic solar-blind UV PD based on STO/$Al_xGa_{1-x}N$ heterostructure for neuromorphic computing. *Appl. Phys. Lett.* **2025**, *126*, 142105.

[3] Zong, B.; Wu, S.; Yang, Y.; Li, Q.; Tao, T.; Mao, S. Smart gas sensors: recent developments and future prospective. *Nano-Micro Lett.* **2024**, *17*, 54.

[4] Yang, H.; Zhang, Y.; Hu, F.; Li, Z.; Wu, D.; Chen, X. Comprehensively modulated sub-attojoule operated optoelectronic synapses for image encryption and inpainting. *ACS Appl. Mater. Interfaces* **2024**, *16*, 57804-57813.

[5] Zhao, S.; Hou, X.; Cheng, Y.; Zhang, Q.; Zhao, J.; Tao, L. Optical synaptic devices with multiple encryption features based on SERS-revealed charge-transfer mechanism. *Adv. Mater.* **2025**, *37*, 2503146.

[6] Yu, Y.; Zhong, M.; Xiong, T.; Yang, J.; Hu, P.; Long, H.; Zhou, Z.; Xin, K.; Liu, Y. Y.; Yang, J.; Qiao, J.; Liu, D.; Wei, Z. Spectrometer-less remote sensing image classification based on gate-tunable van der Waals heterostructures. *Adv. Sci.* **2024**, *11*, 2309781.

[7] Fang, H.; Lu, L.; Pan, Y.; Shi, L.; Chen, W.; Chen, G.; Ou, J.; Zhu, L. Infrared high polarization-sensitive and high-responsivity photodetector based on 2D heterojunction bipolar transistor. *Adv. Opt. Mater.* **2025**, *13*, e01868.

[8] Ma, R.; Tan, Q. H.; Yang, P. Z.; Liu, Y. K.; Wang, Q. J. High-performance and linearly polarized $MoTe_2/ReS_2$ heterojunction phototransistors. *IEEE Electron Device Lett.* **2024**, *45*, 1871-1874.

[9] Lou, Y.; Zhang, S.; Gu, Z.; Wang, N.; Wang, S.; Zhang, Y.; Song, Y. Perovskite single crystals: dimensional control, optoelectronic properties, and applications. *Mater. Today* **2023**, *62*, 225-248.

[10] Huang, W.; Zhang, H.; Tang, J.; Lin, Z.; Guo, T.; Zhou, Y.; Jiang, S.; Hang, P.; Jiao, M.; Zhu, C.; Wang, L.; Yang, D.; Yu, X.; Li, X. A. Self-powered optoelectronic synaptic devices for neuromorphic computing with the lowest energy consumption density. *ACS Photonics* **2024**, *11*, 3095-3104.

[11] Hao, D.; Yang, Z.; Huang, J.; Shan, F. Recent developments of optoelectronic synaptic devices based on metal halide perovskites. *Adv. Funct. Mater.* **2022**, *33*, 2211467.

[12] Li, Y.; Zhang, F.; Wang, S.; Li, D.; Sun, Y.; Gao, Z.; Wu, Z.; Zheng, D. UV–Vis–NIR broadband self-powered Bi_2O_2Se-based semi-vertical heterojunction photodetector with high performance. *Nano Res.* **2026**, *19*, 94908400.

[13] Liang, D.; Jiang, B.; Liu, Z.; Chen, Z.; Gao, Y.; Yang, S.; He, R.; Wang, L.; Ran, J.; Wang, J.; Gao, P.; Li, J.; Liu, Z.; Sun, J.; Wei, T. Quasi van der Waals epitaxy of single crystalline GaN on amorphous SiO_2/Si(100) for monolithic optoelectronic integration. *Adv. Sci.* **2024**, *11*, 2305576.

[14] Pang, X.; Wang, Y.; Zhu, Y.; Zhang, Z.; Xiang, D.; Ge, X.; Wu, H.; Jiang, Y.; Liu, Z.; Liu, X.; Liu, C.; Hu, W.; Zhou, P. Non-volatile rippled-assisted optoelectronic array for all-day motion detection and recognition. *Nat. Commun.* **2024**, *15*, 1613.

[15] Kwon, J.; Jeon, J. B.; Júnior, W. G. G.; Lee, M. G.; Lee, C.; Kim, G.; Song, H.; Cheong, W. H.; Im, S. G.; de Moura, A. F.; Kim, K. M.; Yeom, J. Chiroferromagnetic quantum dots for chiroptical synapse (ChiropS). *Adv. Mater.* **2025**, *37*, 2415366.

[16] Liu, Z.; Zhang, N.; Zhao, X.; Liu, M.; Shi, Y.; Qi, L.; Zou, Y.; Chang, C.; Tan, F.; Li, D.; Li, S. High-performance broadband integrated detection system for multifunctional applications. *ACS Nano* **2025**, *19*, 22414-22425.

[17] Gao, P.; Liu, L.; Tang, Y.; Wang, S.; Zhang, T.; Li, M.; Zhong, B.; Wan, M.; Wang, C.; Wei, Y.; Liao, L.; Wang, J. $MoTe_2/MoSe_2$ vdW Schottky photodetector for polarized photodetection. *Chip* **2025**, *4*, 100147.

[18] Si, M.; Liao, P. Y.; Qiu, G.; Duan, Y.; Ye, P. D. Ferroelectric field-effect transistors based on MoS_2 and $CuInP_2S_6$ two-dimensional van der Waals heterostructure. *ACS Nano* **2018**, *12*, 6700-6705.

[19] Shang, Z.; Liu, L.; Wang, G.; Xu, H.; Cui, Y.; Deng, J.; Lou, Z.; Yan, Y.; Deng, J.; Han, S. T.; Zhai, T.; Wang, X.; Wang, L.; Wang, X. Ferroelectric polarization enhanced optoelectronic synaptic response of a $CuInP_2S_6$ transistor structure. *ACS Nano* **2024**, *18*, 30530-30539.

[20] Liu, J.; Du, F.; Wu, L.; Fang, X. Ferroelectric-configured in-sensor dynamic computing with 2D perovskites for dim object recognition. *Adv. Mater.* **2025**, *38*, e20823.

[21] Jiang, R.; Jia, Y.; Dai, F.; Shi, X.; Gao, Z.; Zhou, Z.; Shi, H.; Wu, Z.; Sun, Y.; Luo, G.; Wang, J.; Wang, F.; Wang, L.; Zhang, J.; Hu, Z.; Chu, J.; Hu, W. Ferroelectric polarization enhanced performance and broadband photodetector for neural network recognition. *Laser Photonics Rev.* **2025**, *19*, e00298.

[22] Wang, Q.; Zhang, H.; Ding, J.; Yang, P.; Liu, Y.; Tan, Q. $CuInP_2Se_6/MoS_2$ heterojunction photodetector with fast response, optical logic, and intelligent image recognition. *J. Mater. Sci. Technol.* **2026**, *270*, 59-67.

[23] Yu, J.; Huang, B.; Yang, S.; Zhang, Y.; Bai, Y.; Song, C.; Ming, W.; Liu, W.; Wang, J.; Li, C.; Wang, Q.; Li, J. Flexoelectric engineering of bulk photovoltaic photodetector. *Nano Lett.* **2024**, *24*, 6337-6343.

[24] Dey, A.; Yan, W.; Balakrishnan, N.; Xie, S.; Kudrynskyi, Z. R.; Makarovskiy, O.; Yan, F.; Wang, K.; Patanè, A. Memristive effects due to charge transfer in graphene gated through ferroelectric $CuInP_2S_6$. *2D Mater.* **2022**, *9*, 035003.

[25] Li, K.; He, T.; Guo, N.; Xu, T.; Fu, X.; Wang, F.; Xu, H.; Li, G.; Liu, S.; Deng, K.; Xiao, Y.; Miao, J.; Hu, W. Light-triggered and polarity-switchable homojunctions for optoelectronic logic devices. *Adv. Opt. Mater.* **2023**, *11*, 2202379.

[26] Zhang, B. Y.; Liu, T.; Meng, B.; Li, X.; Liang, G.; Hu, X.; Wang, Q. J. Broadband high photoresponse from pure monolayer graphene photodetector. *Nat. Commun.* **2013**, *4*, 1811.

[27] Bie, Y. Q.; Grosso, G.; Heuck, M.; Furchi, M. M.; Cao, Y.; Zheng, J.; Bunandar, D.; Navarro-Moratalla, E.; Zhou, L.; Efetov, D. K.; Taniguchi, T.; Watanabe, K.; Kong, J.; Englund, D.; Jarillo-Herrero, P. A $MoTe_2$-based light-emitting diode and photodetector for silicon photonic integrated circuits. *Nat. Nanotechnol.* **2017**, *12*, 1124-1129.

[28] Yu, X.; Yu, P.; Wu, D.; Singh, B.; Zeng, Q.; Lin, H.; Zhou, W.; Lin, J.; Suenaga, K.; Liu, Z.; Wang, Q. J. Atomically thin noble metal dichalcogenide: a broadband mid-infrared semiconductor. *Nat. Commun.* **2018**, *9*, 1545.

[29] Mao, X.; Fu, J.; Chen, C.; Li, Y.; Liu, H.; Gong, M.; Zeng, H. Nonvolatile electric control of exciton complexes in monolayer $MoSe_2$ with two-dimensional ferroelectric $CuInP_2S_6$. *ACS Appl. Mater. Interfaces* **2021**, *13*, 24250-24257.

[30] Wang, S.; Fan, N.; Zhou, Z.; Hu, Y.; Hui, Q.; Li, Q.; Xue, J.; Zhou, Z.; Feng, Z.; Yan, Q.; Weng, Y.; Tang, R.; Zheng, F.; Fan, R.; Xu, B.; Fang, L.; You, L. Self-enhancing photoelectrochemical properties in van der Waals ferroelectric $CuInP_2S_6$ by photoassisted acid hydrolysis. *ACS Appl. Mater. Interfaces* **2022**, *14*, 40126-40135.

[31] Zhang, X.; Xiao, C.; Zhang, Z.; Dong, L.; Pan, H.; Cao, C.; Yang, S. A.; Wei, S. H.; Lu, Y. Origin of versatile polarization state in $CuInP_2S_6$. *Phys. Rev. B* **2023**, *108*, L161406.

[32] Liu, C. H.; Chang, Y. C.; Norris, T. B.; Zhong, Z. G. Graphene photodetectors with ultra-broadband and high responsivity at room temperature. *Nat. Nanotechnol.* **2014**, *9*, 273-278.

[33] Assefa, S.; Xia, F.; Vlasov, Y. A. Reinventing germanium avalanche photodetector for nanophotonic on-chip optical interconnects. *Nature* **2010**, *464*, 80-84.

[34] Li, S.; Zhou, J.; Xiong, J.; Yang, S.; Zhang, J.; Fan, W.; Li, J. Two dimensional $CuInP_2S_6$/h-BN/$MoTe_2$ van der Waals heterostructure phototransistors with double gate control. *J. Mater. Chem. C* **2025**, *13*, 2378-2386.

[35] Zhao, Z.; Xu, K.; Ryu, H.; Zhu, W. Strong temperature effect on the ferroelectric properties of $CuInP_2S_6$ and its heterostructures. *ACS Appl. Mater. Interfaces* **2020**, *12*, 51820-51826.

[36] Ma, R.; Tan, Q. H.; Yang, P. Z.; Liu, Y. K.; Wang, Q. J. High performance photodetector based on few-layer $MoTe_2$/$CdS_{0.42}Se_{0.58}$ flake heterojunction. *Front. Phys.* **2024**, *19*, 43204.

[37] Ng, R. O. L.; D, S. Electrodeposited polycrystalline thin films of cadmium chalcogenides for backwall photoelectrochemical cells. *Sol. Energy Mater.* **1984**, *11*, 319-328.

[38] Ren, L.; Tan, Q. H.; Gao, K. P.; Yang, P. Z.; Wang, Q. J.; Liu, Y. K. Constructing high-quality 1D nano/microwire hybrid structure for high-performance photodetectors based on CdSe nanobelt/perovskite microwire. *Nanophotonics* **2023**, *12*, 1347-1357.

[39] Yang, S.; Tongay, S.; Li, Y.; Yue, Q.; Xia, J. B.; Li, S. S.; Li, J.; Wei, S. H. Layer-dependent electrical and optoelectronic responses of $ReSe_2$ nanosheet transistors. *Nanoscale* **2014**, *6*, 7226-7231.

[40] Ma, X.; Wang, Z.; Qin, Q.; Chen, J.; Liu, X.; Zou, F.; Xu, Z.; Chen, W.; Li, G.; Li, Y.; Zhai, T.; Li, L.; Simultaneous AoLP and DoLP detection in a bias-switchable $PdSe_2$/MoS_2/$PdSe_2$ heterojunction for polarization discrimination. *Adv. Mater.* **2025**, *37*, 2500572.

[41] Ren, X.; An, X.; He, X.; Feng, W.; Wang, B.; Chen, W.; Gao, F.; Zhang, J.; Hu, P. Low-temperature growth of high-quality Bi_2O_2Se nanosheets enabling weak-light detection with ultralow dark current. *Nano Lett.* **2026**, *26*, 2307-2315.

[42] Luo, L. B.; Wang, D.; Xie, C.; Hu, J. G.; Zhao, X. Y.; Liang, F. X. $PdSe_2$ multilayer on germanium nanocones array with light trapping effect for sensitive infrared photodetector and image sensing application. *Adv. Funct. Mater.* **2019**, *29*, 1900849.

[43] Ye, L.; Wang, P.; Luo, W.; Gong, F.; Liao, L.; Liu, T.; Tong, L.; Zang, J.; Xu, J.; Hu, W. Highly polarization sensitive infrared photodetector based on black phosphorus-on-WSe_2 photogate vertical heterostructure. *Nano Energy* **2017**, *37*, 53-60.

[44] Zhang, Q.; Tan, Q.; Ding, J.; Feng, X.; Yang, P.; Liu, Y.; Wang, Q. High performance dual-band Bi_2O_2Se/CdS heterojunction photodetector for encrypted optical communication. *Nano Res.* **2025**, *18*, 94907550.

[45] Pi, H.; Ding, C.; Liu, Y.; Yang, H.; Li, G.; Chen, B.; Cui, Y. An ultra-low dark current $AgBiS_2$ CQDs NIR photodetector using ZnO/MXenes bilayer electron transport layer for image sensor. *Nano Res.* **2026**, *19*, 94908699.

[46] Ma, L.; Hu, W.; Zhang, Q.; Ren, P.; Zhuang, X.; Zhou, H.; Xu, J.; Li, H.; Shan, Z.; Wang, X.; Liao, L.; Xu, H. Q.; Pan, A. Room-temperature near-infrared photodetectors based on single heterojunction nanowires. *Nano Lett.* **2014**, *14*, 694-698.

[47] Liu, Z.; Peng, S.; Zhang, Q.; Li, M.; Xiao, Y.; Gao, Y.; Ge, F.; Wang, X.; Huang, Q.; Xue, J. Fabrication of high-responsivity FET photodetector with $Ti_3C_2Cl_2$ MXene irradiated with 100 keV N ions. *Nano Res.* **2026**, *19*, 94908342.

[48] Wang, J.; Bai, G.; Hu, Y.; Yin, Z.; Tang, A. Mn-doping-engineered $CsBi_3I_{10}$ lead-free perovskite photodetectors for high-performance blood oxygen monitoring. *Nano Res.* **2026**, *19*, 94908478.

[49] Ren, W. P.; Tan, Q. H.; Wang, Q. J.; Liu, Y. K. Hybrid organolead halide perovskite microwire arrays/single CdSe nanobelt for a high-performance photodetector. *Chem. Eng. J.* **2021**, *406*, 126779.

[50] Xiang, Z. L.; Tan, Q. H.; Zhu, T.; Yang, P. Z.; Liu, Y. P.; Liu, Y. K.; Wang, Q. J. High-performance 1D $CsPbBr_3$/CdS photodetectors. *Rare Met.* **2024**, *43*, 5932-5942.

[51] Wang, F.; Zhang, T.; Xie, R.; Wang, Z.; Hu, W. How to characterize figures of merit of two-dimensional photodetectors. *Nat. Commun.* **2023**, *14*, 2224.

[52] Zeng, L.; Lin, S.; Lou, Z.; Yuan, H.; Long, H.; Li, Y.; Lu, W.; Lau, S. P.; Wu, D.; Tsang, Y. H. Ultrafast and sensitive photodetector based on a $PtSe_2$/silicon nanowire array heterojunction with a multiband spectral response from 200 to 1550 nm. *NPG Asia Mater.* **2018**, *10*, 352-362.

[53] Pecunia, V.; Anthopoulos, T. D.; Armin, T.; Bouthinon, B.; Caironi-Gomez, M.; Chen, Y.; Cho, K.; Clegg, C.; Fang, X.; Fendel, P.; Fowler, B.; Gelinck, G.; Gottlob, H.; Guyot-Sionnest, P.; Hannebauer, R.; Hernandez-Sosa, G.; Hersam, M. C.; Hirsch, L.; Ho, J. C.; Isikgor, F. H.; Joimel, J.; Kim, H. J.; Konstantatos, G.; Labram, J.; Lemme, M. C.; Leo, K.; Lhuillier, E.; Lidorikis, E.; Loi, M. A.; Malinowski, P. E.; Merken, P.; Mueller, T.; Nasrollahi, B.; Natali, D.; Ng, T. N.; Nguyen, T. Q.; Park, S. K.; Peng, L. M.; Samori, P.; Sargent, E. H.; Shen, L.; Shorubalko, I.; Sonar, P.; Stranks, S. D.; Tedde, S. F.; Vandewal, K.; Verhaegen, K.; Walia, S.; Yan, F.; Yokota, T.; Zhang, F. Guidelines for accurate evaluation of photodetectors based on emerging semiconductor technologies. *Nat. Photonics* **2025**, *19*, 1178-1188.

[54] Ma, R. R.; Xu, D. D.; Guan, Z.; Deng, X.; Yue, F.; Huang, R.; Chen, Y.; Zhong, N.; Xiang, P. H.; Duan, C. G. High-speed ultraviolet photodetectors based on 2D layered $CuInP_2S_6$ nanoflakes. *Appl. Phys. Lett.* **2020**, *117*, 131102.

[55] Qiu, D.; Hou, P.; Wang, J.; Ouyang, X. Photoconductivity, pyroconductivity, and pyroelectricity effects in photodetection of layer-structured $CuInP_2S_6$/MoS_2 heterojunction. *Appl. Phys. Lett.* **2023**, *123*, 042105.

[56] Chen, X.; Zhang, Q.; Peng, J.; Gao, W.; Yang, M.; Yao, P.; Liang, Y.; Xiao, Y.; Zheng, Z.; Li, J. B. Ideal photodetector based on WS_2/$CuInP_2S_6$ heterostructure by combining band engineering and ferroelectric modulation. *ACS Appl. Mater. Interfaces* **2024**, *16*, 13927-13937.

[57] Wang, D.; Wu, Q.; Shan, K.; Han, M.; Jiang, W.; Meng, W.; Zhang, Y.; Xiong, W. Enhanced photoelectric performance of Bi_2O_2Se/$CuInP_2S_6$ heterojunction via ferroelectric polarization in two-dimensional $CuInP_2S_6$. *Phys. Chem. Chem. Phys.* **2024**, *26*, 21357-21364.

[58] Tan, C.; Wu, H.; Lin, Z.; Yang, L.; Wang, Z. 2D reconfigurable memtransistor for high-performance dual-mode memory and broadband photodetection. *Adv. Funct. Mater.* **2025**, *35*, 2415360.

[59] Wu, H.; Lin, Z.; Chen, X.; Tan, C.; Hu, G.; Wang, Z. Wide wavelength band responsive In_2Se_3/CIPS heterojunction for polarization imaging enhancement in image fusion. *ACS Appl. Mater. Interfaces* **2025**, *17*, 37035-37042.

[60] Ma, R.; Tan, Q. H.; Liu, Y. K.; Wang, Q. J. High performance photodetector based on CdS/$CdS_{0.42}Se_{0.58}$ nanobelts heterojunction. *J. Phys. Condens. Mat.* **2024**, *36*, 125305.